HHS Public Access

Author manuscript

J Steroid Biochem Mol Biol. Author manuscript; available in PMC 2019 July 01.

Published in final edited form as:

J Steroid Biochem Mol Biol. 2018 July ; 181: 11–19. doi:10.1016/j.jsbmb.2018.02.009.

Testosterone Complex and Non-Steroidal Ligands of Human Aromatase

Debashis Ghosh[*], **Chinaza Egbuta**[‡], and **Jessica Lo**

Department of Pharmacology, State University of New York Upstate Medical University, Syracuse, New York 13210

Abstract

Cytochrome P450 aromatase (AROM) catalyzes the biosynthesis of estrogen from androgen. Previously crystal structures of human AROM in complex with the substrate androstenedione, and inhibitors exemestane, as well as the newly designed steroidal compounds, have been reported. Here we report the first crystal structure of testosterone complex of human placental AROM. Testosterone binds at the androgen-specific heme distal pocket. The polar and hydrophobic interactions with the surrounding residues resemble the interactions observed for other ligands. The heme proximal region comprises the intermolecular interface in AROM, and also the putative interaction surface of its redox partner cytochrome P450 reductase. Unreported previously, the proximal region is characterized by a large surface cavity, unlike most known P450's. Using five best X-ray data sets from androstenedione and testosterone complexes of AROM, we now unequivocally show the presence of an unexplained ligand electron density inside the proximal cavity. The density is interpreted as ordered five ethylene glycol units of polyethylene glycols used as a solvent for steroids and also in crystallization. Interestingly, polyethylene glycol exhibits weak inhibition of AROM enzyme activity in a time dependent manner. Besides its critical role in the redox partner coupling and electron transfer process, the proximal cavity possibly serves as the interaction site for other molecules that may have regulatory effects on AROM activity. In addition, the new data also reveal a previously unidentified water channel linking the active site to the lipid interface. The channel could be the predicted passage for water molecules involved in catalysis.

Graphical abstract

[*]To whom correspondence should be addressed: Prof. Debashis Ghosh, Department of Pharmacology, SUNY Upstate Medical University, 750 East Adams Street, Syracuse, NY 13210, Telephone: (315)-464-9677, Fax: (315)-464-8014, ghoshd@upstate.edu.
[‡]Present address: Departments of Medicine & Pathology, New York University School of Medicine 550 First Avenue, New York, NY 10016

Author contribution

D.G. conceived, designed, planned and supervised experiments. D.G. performed data collection, data processing, refinement, and analysis, and wrote the manuscript. C.E. performed data processing, refinement and analysis. J.L. performed data collection, data processing and analysis. C.E. and J.L. assisted in writing the manuscript.

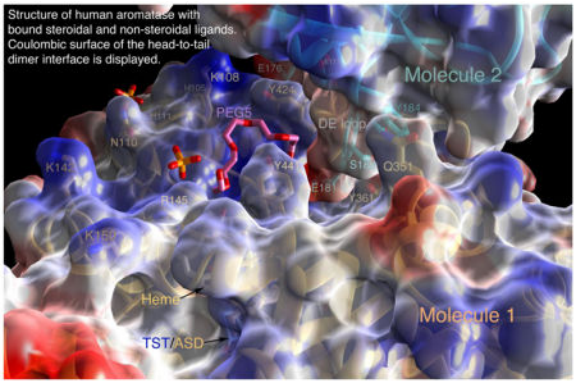

Keywords

aromatase; cytochrome P450; estrogen; estradiol; testosterone; androstenedione; structural biology

1. Introduction

Human cytochrome P450 aromatase, (AROM; *CYP19A1*; 503 amino acid) exhibits high substrate specificity in catalyzing the synthesis of estrogen from androgenic precursors [1]. The enzyme is the product of the *CYP19A1* gene, which has one family and one subfamily, and is an integral membrane hemeprotein of the endoplasmic reticulum. Inhibition of estrogen biosynthesis by AROM inhibitors (AI) constitutes one of the foremost therapies for postmenopausal estrogen-dependent breast cancer today.

Cytochrome P450s in general catalyze the metabolism of a wide variety of endogenous and xenobiotic compounds, and drugs with low substrate specificities [2]. AROM, on the contrary, uses with high specificity androstenedione (ASD), testosterone (TST), and 16α-hydroxytestosterone (all with the same androgen backbone) as substrates converting them to estrone (E1), 17β-estradiol (E2), and estriol (E3) (all with the same estrogen backbone), respectively [3]. Because of its unique hydroxylation reaction that involves a carbon-carbon bond cleavage and a ring aromatization, AROM has been a target of biochemical and biophysical investigations for the past 50 years [1, 3–9]. Recent advancement on structure and function of AROM in complex with the natural substrate ASD and steroidal inhibitors have provided the molecular basis for its substrate specificity, reaction mechanism, steroidal passage, vibrational modes, trans-membrane integration and oligomeric state [10–15].

For the three-step hydroxylation and aromatization reaction [16], AROM couples with cytochrome P450 reductase (CPR) that supplies the electrons necessary for the process. There is strong evidence that CPR couples to P450's with its FMN-binding domain closest to the heme-proximal interface [17]. The heme proximal site of AROM could also be involved in binding with other protein partners, such as kinases and phosphatases that have been proposed to modulate AROM activity [18, 19]. Furthermore, inhibition kinetics of non-steroidal compounds [20] and molecular mechanics/dynamics analyses have suggested the presence of additional ligand binding sites [21]. Normal modes analysis has indicated opening and closing of channels and passages due to AROM's breathing motion [14].

Here utilizing new X-ray data on the crystals of human placental AROM (pAROM) we show that the substrate TST, a more potent androgen than ASD, binds at the heme-distal active site with substrate-specific interactions with the surrounding side chains, in a similar manner observed for the ASD complex. Unreported previously, the heme proximal site harbors a scaffold large enough to accommodate an interaction partner and/or a non-steroidal molecule, unlike most cytochrome P450s, and that intermolecular interaction via the proximal cavity could influence AROM enzymatic activity. Furthermore, we identify a previously unrecognized water channel that extends from the active site to the protein exterior and could be the transport route for catalytic waters.

2. Material and methods

2.1 Chemicals

Emulgen913 was purchased from Desert Biologicals (Phoenix, AZ). n-dodecyl-β-D-maltopyranoside (BDM) was purchased from Affymetrix (Cleveland, OH). [1β-^{3}H, 4-^{14}C] androstenedione was purchased from Perkin Elmer (Waltham, MA). Polyethylene glycol (PEG) 550, and all other chemicals were purchased from Sigma Aldrich (St. Louis, MO).

2.2 Purification from human placenta

Human placental pAROM was purified from the microsomal fraction of term placenta with a monoclonal antibody 3-2C2 column, using a well-established protocol [22, 23]. A recombinant form of the human enzyme expressed in bacteria (rAROM) has also been purified and crystallized [15].

2.3 Preparation and crystallization of pAROM complexes

The specific activity of the purified pAROM in *n*-dodecyl-β-d-maltopyranoside (BDM) ranged from 30 to 50 nmol min^{-1} mg^{-1} over many independent measurements performed in triplicate. Crystallization of the pAROM-ASD complex has already been described [10]. The pAROM-TST complex was prepared by incubating 20 mM DTT and 100 μM of TST (from a stock of 5 mM TST dissolved in 100% PEG550) with the purified protein solution in 100 mM KPO_4 pH 7.4, containing 20% glycerol, 0.5 μM TST, 0.1mM EDTA, and 1.0mM BDM. The TST complex was then concentrated to about 30 mg/mL and crystallized (with PEG4000) using the same methodology previously described for the ASD complex. Initial concentrations of PEGs 550 and 4000 in the crystallization solution were roughly 1% and 10%, respectively.

2.4 X-ray crystallography

Several new diffraction data sets on the ASD and TST complexes were collected on the synchrotron X-ray beam line 19-ID at the Advanced Photon Source, Argonne National Laboratory, Argonne, IL. The results from five highest resolution data sets (four ASD numbered 1 through 4, and one TST complexes of pAROM) are being presented here. Amongst these, only the ASD1 complex at 2.90 Å and 2.75 Å resolutions (PDB IDs: 3EQM, 3S79, respectively) has already been reported [10, 24]. All data sets were processed with HKL2000 [25]. The data collection and processing parameters are provided in Table 1. The crystals of pAROM-TST and -ASD complexes were all isomorphous to the published

pAROM-ASD complex [10, 24]. Refinement and model building were performed with Refmac5 [26] and Coot [27], respectively. A difference (Fo-Fc) omit map was used to model the bound TST molecule in the active site. In addition, two separate electron densities were identified in the difference omit maps contoured at 4.0–4.5σ levels (see results for full description). The first density was located in the heme-proximal cavity, and the other behind the substrate, near S314 of I-helix. The density in the heme-proximal cavity was modeled as five units of polyethylene glycol (PEG5) using the map for pAROM-ASD1 complex. The model was then refined against this 2.75Å resolution data. The second density was modeled as a network of 7 water molecules involved in hydrogen bond interactions with each other and also with protein atoms. The water oxygen atoms were first refined against each individual data set. The refined water molecules from each complex were superimposed to generate a final model by optimizing the hydrogen bond geometries. The refinement results are summarized in Table 1. The final model of pAROM-TST complex contained 452 amino-acid residues, a heme group, one TST molecule, and seven water molecules. Forty-four N-terminal and 7 C-terminal residues were not included in the model and refinement because of weakness of their electron densities [10]. The model for the N-terminal helix was adopted from a previous work in which residues N12 to T44 were built using partially visible weak experimental electron density, but not included in refinement [14]. All five refined sets of coordinates and structure factors have been deposited with the RCSB Protein Data Bank (see Table 1 for the PDB ID codes) and are now readily available.

2.5 Calculation of cavity volume and interface surface area

The three-dimensional structure of ASD/TST-bound human pAROM with its N-terminal helix [10, 14] was analyzed in MOE2015.10 Site Finder application [28] to determine ligand-binding cavities. Removal of the substrate from its experimentally observed binding site prior to computational analysis validated the method. In addition, the active site volume computed by Site Finder was validated against the previously reported value [10]. The binding cavity volumes were computed with Q-Site Finder [29] and CASTp Server [30]. However, the Q-Site Finder computation appeared to be more conservative estimates and consistent with the internal control of active site volume, and hence was the one used for further analysis. Visualization was done with the UCSF Chimera package [31].

The solvent-accessible surface areas of the pAROM monomer and homo dimer were computed with PYMOL [32] and MOE2015.10 using a solvent radius of 1.5Å. The interaction surface between the D-E loop of one pAROM molecule and the heme-proximal surface of another was determined by calculating the surface areas of the pAROM monomer and the dimer.

2.6 Assay of AROM inhibition by PEG550

Time-dependent inhibition of pAROM by PEG550 was measured by first pre-incubating the enzyme as follows: at 5% and 10% of PEG550 for 16 hours each (data not shown), and at a fixed concentration (10%) of PEG550 for 0 to 70 hour. The specific activity of each sample was determined with the tritiated water release method following the ^{3}H1β androstenedione-to-estrone aromatization reaction [23]. Assays were performed in the presence of [1β-^{3}H,

4-^{14}C] androstenedione, excess purified rat CPR and 5mM NADPH in the reduced form. Any inconsistent data were re-measured and outliers were excluded from the averaging.

2.7 UV/Visible Spectrophotometry

Following pre-incubation, pAROM integrity was determined by measuring the Soret peak on the Cary50 UV-visible spectrophotometer with a 1ml quartz cuvette of 1cm path length. The purified protein solution was scanned across the visible light range (from 250nm to 650nm) in a Cary50 UV-visible spectrophotometer using a 1ml quartz cuvette of 1cm path length in order to determine the pAROM integrity in the presence of PEG550. 1μL of each sample was then reconstituted in DLPC and pAROM activity was measured in quadruplicate. The integrated area of each Soret peak was determined by the area under the curve analysis using GraphPad Prism® 6.0, Macintosh version (GraphPad Software, La Jolla, California, USA, www.graphpad.com). The area under the curve is determined using the trapezoid rule. The trapezoid rule determines the area under the curve by assuming that the curve is composed trapezoids and calculates the area of each trapezoid. This method takes into account both the height and broadness of the Soret peak.

2.8 Effect of 10% PEG550 on pAROM activity as a function of time

The percent reduction of pAROM activity by PEG550 was determined by one-phase exponential decay curve fitting on GraphPad Prism®. The following model: $Y = (Y_0 - Plateau)*exp(-K*X) + Plateau$ was used to generate the best-fit value. Y_0 is the Y (percent activity) when X (time) is zero. *Plateau* is the Y value at infinite time, expressed in the same units as Y. K is the rate constant, expressed in reciprocal of the X-axis (time) unit.

3. Results

3.1 TST complex of pAROM

The structure of the active site with the bound TST is shown in Figure 1. The bound TST is shown in Figure 1A within its unbiased (prior to inclusion of TST in the refinement) difference electron density map, contoured at 4.0 σ (standard deviation). TST binds with its 17β-hydroxyl oxygen receiving a hydrogen bond (2.7Å) from the backbone amide −NH of M374 while making a polar contact (3.3Å) with the R115 guanidinium group. The 17β-hydroxyl proton possibly orients itself towards the backbone carbonyl oxygen (3.6 Å) of M374, which would constitute a rather long hydrogen bond. Superposition of the crystal structures (Figure 1B) of the ASD and TST complexes shows that the root mean square deviation between the Cα atom pairs is 0.2Å suggesting that the structures are identical within the limits of errors. The deviation between the two substrates is highest at C17 of the D-ring - 0.4 Å, slightly more than the random positional error limit. As a result, the 17β-hydroxyl oxygen is marginally closer to the M374 backbone carbonyl. The 3-keto oxygen of the A-ring accepts a hydrogen bond from the protonated D309, and C19 is at a distance of 3.8Å from the heme iron (Figure 1A). These distances are similar to the ASD complex within ±0.2Å. Proposed protonation of D309 at crystallization pH of 7.4 [10] has since been experimentally confirmed [33].

Like in the ASD complex structure, the bound TST molecule is snugly surrounded from its α-face by large hydrophobic side chains W224, F221, F134, I133, V370 and M374 (Figure 1A, B) that mold the active site cleft to precisely complement the TST structure and puckering of its backbone. These interactions, together with the polar contacts described above and the contact at C19 with heme-moiety on the β-face, account for the molecular basis of androgenic specificity of AROM.

3.2 A ligand-binding scaffold at the heme-proximal site

X-ray data and refinement results for 1 TST and 4 ASD complexes are summarized in Table 1. The data for the pAROM-ASD1 complex without the ligand is published [24] (PDB ID: 3S79); others are new and unpublished. All co-ordinates and diffraction data have been deposited with the Protein Data Bank; see Table 1 for the PDB ID codes. Difference (Fobs-Fcal) electron density maps from these five best resolution data sets contoured at 4.0 to 4.5σ consistently show a strong density suitable for a small molecule at the heme proximal cavity (Figure 2). This sigma level for signal-to-noise filtering is determined by simultaneously calculating the unbiased (omit) difference electron density for the bound substrate ASD/TST as the control. A worm-like shape of the density suggests that a non-steroidal molecule, a polymer such as PEG or a peptide would be appropriate as the bound ligand. Five units of PEG, PEG5, is modeled inside the well-defined and continuous portion of the electron density that is present in all five maps and refined against highest resolution data set (2.75Å). In addition, two isolated densities in close proximity suitable for a water oxygen atom and a phosphate ion are also modeled (supplemental Figure S1). PEG5 makes several hydrogen bond-forming contacts with the protein and solvent atoms (Figure S1) by accepting a proton in each case. One of them is with the K440 side chain and another with G433 backbone amide NH.

The modeling assumes that only a short pentameric segment of PEG550 or PEG4000, used as a solvent for the substrate or as the crystallizing agent, respectively, is tightly bound at the proximal cavity and hence has a defined electron density. The rest of the bound PEG molecule in all likelihood is dynamically disordered in the bulk solvent space. In fact, both ends of the modeled PEG5 could be extended into the empty space representing bulk, disordered solvent. Interestingly, there are other pieces of yet unexplained electron densities at the ≥4σ level (Figure 2) that are disconnected from the main density and could conceivably represent sections of a longer PEG molecule not modeled.

3.3 The heme-proximal cavity unique to AROM

In addition to the PEG binding scaffold, the proximal cavity is also the dimerization interface for both pAROM and recombinant rAROM crystal structures, which are identical [10, 12, 15]. This head-to-tail association occurs through the heme-proximal cavity of one molecule and the loop D-E between helices D and E of the adjacent molecule as illustrated in Figure 3, and previously described [12, 15], creating an AROM polymer chain that extends throughout the crystal. Two such polymer chains associate about a 2-fold rotational axis generating the $P3_221$ space group symmetry [12]. Thus, interestingly, the proximal cavity appears to have two compartments, one that snugs the D–E loop region of the neighboring molecule, and the other that scaffolds the PEG5 ligand (Figure 3). At this

interface, the intermolecular association is governed not only by electrostatics but also by shape complementarity of the surfaces as previously described [12]. An interfacial area of 1475Å^2 is buried by the intermolecular contact, a number comparable to physiologically meaningful interactions, such as antigen-antibody recognition [34].

Computation of the volume (Table 2) shows that such a well-defined proximal cleft is rather unusual among known P450s. An exhaustive search of all P450s in the protein data bank confirms that AROM has one of the largest proximal cavities. Some of the close competitors and human P450s in the steroidogenic pathways are shown in Table 2. Many bacterial and mammalian P450s listed in Table 2 have no appreciable indentation at the proximal surface at all. The known volume of the tight active site cleft is used as a control for validation of the computations. Surprisingly, the proximal cavity of AROM appears to about 50% larger than its active site volume.

3.4 PEG550 reduces enzyme activity in a time-dependent manner

In order to determine the effect of PEG550 on the enzyme function, if any, we measured the enzyme activity as functions of PEG550 concentration and time of incubation. However, the enzyme at 0.3mg/ml, the optimal concentration for quantification of its catalytic and spectral properties, precipitates at PEG550 concentrations above 10% evidenced by gradual loss of the characteristic Soret peak at 393 nm (data not shown). Therefore, we have measured the change in its catalytic activity at 10% PEG550 (182 mM) as a function of time. To monitor the integrity of pAROM in solution, we also record the Soret peak at each time point and use the integrated area under the peak as a measure of pAROM integrity retained in solution. The results are shown in Figure 4. Figure 4A shows that in the presence of 10% PEG550 the specific activity of pAROM gradually reduces and plateaus around 80% after about 70 hours. The lower panel (Figure 4B) is a superposition of the absorption spectra of pAROM recorded at each time point between 0 and 72 hour. The integrated intensity of the Soret peak at 393 nm, characteristic of the substrate-bound high spin ferric state, is maintained at 100% while the activity reduces in a time dependent manner (Figure 4B). Least squares fit to the data yields a *Plateau* value of 81.7% for a maximum activity at time zero (Y_0) of 100% and a rate constant K of 0.0582 hr^{-1} (see material and methods).

3.5 A backdoor water channel with catalytic implications

Shown in Figure 5 is a superposition of five unbiased difference electron density maps (contoured at 4.0–4.5σ) that delineate the previously unidentified water channel, and extends from the active site to opening to the lipid interface. Also shown are seven water molecules modeled within the electron density and their polar contacts. The final oxygen positions are derived from averages of the five individually refined models. The channel is too narrow to model the electron density with any other carbon-containing ligand, such as PEG, that results in steric clashes (≤3Å) with protein atoms. Water molecules make only hydrogen bond forming contacts among themselves and with the protein atoms, thereby establishing unequivocally that this is a water-filled channel or aqueduct. This “backdoor” channel is distinctly different from the “active site access” or “front door” channel described previously [10]. Another view of these two channels can be seen in Figure 2. Their relative orientations

and locations with respect to the lipid bilayer with pAROM as a membrane-integrated molecule [14] is shown in Figure 6.

While the access channel is presumably for the passage of substrate/product to/from the active site and accommodates water molecules for the protonation of D309 as well as enolization of 3-keto [10], the backdoor channel could be involved in the delivery of previously postulated “catalytic water’ between T310-Oγ H and the Fe-peroxy/hydroperoxy intermediate for H2β extraction and aromatization [10]. The inner end of the channel makes hydrogen-bonding contacts with the I-helix at S314, which is one turn away from T310. The channel weaves through the narrow opening delineated by the I-helix (293–324), the heme group, the C terminus of helix K (354–366), the loop between helix K and β3 (373–376), and helix K’ (398–404), reaching N75 side chain of helix A and H475 of β8 (Figure 5). Both these residues are at the exterior of the molecule and at the lipid interface, as helix A and β8 are at least partially embedded in the lipid bilayer (Figure 6; β8 is hidden behind β7) [14]. Furthermore, H475 has consistently been found with a bound phosphate ion. The channel could, thus, form a route for the passage of water molecules between the membrane interface and the active site.

4. Discussion

We use new structural data to show that the substrate TST, a more potent androgen than ASD, binds at the heme-distal active site with substrate-specific interactions with the surrounding side chains, in a similar manner observed for the ASD complex. The 17β-OH group of TST is accommodated via two polar contacts with protein atoms and the C17 carbon atom has the highest deviation from the corresponding carbon atom in the ASD complex. Unreported previously, we show that the heme proximal site harbors a scaffold that is capable of binding and/or stably interacting with a ligand such as PEG or other molecules, and that this surface cavity is larger in area and volume than most other P450’s. Furthermore, it appears that the proximal cavity is divided into two compartments, one that accommodates the ligand density, and the other that forms the intermolecular interface (Figure 3). Although we have demonstrated that this head-to-tail polymeric association of AROM utilizing the crystal symmetry has built-in flexibility to form a multimeric association capable of inserting itself into the lipid bilayer [14], the biological and physiological implications of such crystal packing interactions, if any, remain to be elucidated. Interestingly, the first compartment is large enough to bind an interaction partner raising the possibility that the proximal cavity as a whole could furnish a three-way interaction surface. The X-ray data presented suggests that multiple subunits of a larger polymeric molecule such as PEG can fit into the cavity while keeping the intermolecular association intact. This is the unequivocal evidence that two interaction partners could simultaneously bind at the proximal interface without having to displace each other in the process. However, it is also possible that the D–E loop to proximal cavity intermolecular association has no physiological significance and the redox partner CPR binds P450s at the proximal interface occupying the entire proximal site.

Functional implications notwithstanding, the intermolecular contact appears to shield the Y361 side chain (Figure 3) from being accessible for regulation by phosphorylation/

dephosphorylation as has been proposed [18, 19]. It is, therefore, likely that Src kinase and PTP1B phosphatase bind to an AROM monomer with open proximal sites and an accessible Y361. This scenario is consistent with the notion that a dynamic equilibrium between AROM monomers and oligomers exists in solution, and that oligomerization of AROM is concentration dependent – the lower order is favored at lower concentrations [15]. The catalytic residues of the kinase and the phosphatase would probably have closer interactions with the second compartment adjacent to Y361, while the FMN moiety of CPR could bind at the first, near the PEG5 site in close proximity to heme. Again, a direct one-to-one association between AROM and any of these functional partners using most of the proximal interface cannot be ruled out.

A PEG pentamer at the proximal ligand site is consistent with the electron density map as well as binding interactions. Not only all human placental pAROM crystals examined to date exhibit the density, the crystals of rAROM expressed in bacteria [15] do as well. PEG used in crystallization and as a solvent for steroidal ligands is the only logical choice that explains the experimental data. Given the location of the PEG binding site that borders the bulk solvent boundary, it is highly plausible that only a short section of the polymer chain lodged within the cavity will be relatively “static” and have defined electron density, while the rest will be dynamically disordered within the bulk solvent-detergent continuum. Although the data suggests that PEG at best is a weak inhibitor of pAROM (maximum inhibition of about 20% at 182 mM), the time-dependent nature of non-covalent binding at a non-substrate site could be indicative of conformational changes and/or allostery, as others previously noted [35, 36]. A ligand at this site could prevent or destabilize the formation of the redox complex, and/or interfere with the transfer of electrons, unlike a self-contained catalytic system.

PEG5 makes polar contacts with the K440 side chain and G433 backbone NH (supplemental Figure S1). We have shown that K440Q mutation nearly abolishes the enzyme activity and the presence of the positive charge here could be critical to the stability of the region [15]. K440 is the first residue of helix L, at the end of a long loop between residues 419 to 439 between the K” and L helices. This loop contains several key residues including R435, involved in heme coordination, and C437, the ligand to heme iron. The loop is stabilized by an intra-strand hydrogen bond F430CO---HNC437 and a hydrogen bond between the K440 side chain and G431 carbonyl. Therefore, PEG binding here could directly influence AROM activity by introducing structural/chemical instability and by shielding the positive electrostatic potential that drives the AROM-CPR coupling [37]. Nevertheless, whether a ligand at the proximal cavity of AROM can allosterically influence catalysis at the distal substrate site is only a matter of conjecture at this point. A high-affinity ligand at this PEG binding site is necessary in order to address this question. On a related note, the proximal cavity region has shown modest fluctuations in our previous computational work [14]. Therefore, some conformational flexibility of this area is likely, and possibly is conducive to its interaction and binding with molecular partners via “induced fit” mechanisms that could result in alterations of conformation of the proximal cavity region depending on the ligand.

All P450 catalysis requires water molecules in and out of the active site. Water channels or aqueducts have thus been identified in many structures of P450s [38, 39]. We have

previously located an “active site access” or “front door” channel, presumably for the passage of substrate/product to/from the active site [10] (Figure 6). This channel also accommodates water molecules and a proton relay network for the protonation of D309 as well as enolizalation of 3-keto [10]. The newly discovered “backdoor” channel is located on the opposite side of the catalytic cleft and starts near S314 of I-helix (Figures 2 and 5). The channel is linked to S314 side chain by a hydrogen bond while donating the proton to the T310 carbonyl (Figure 5). The backdoor channel could, thus, be involved in the passage of previously postulated “catalytic water’ between T310-OγH and the Fe-peroxy/hydroperoxy intermediate for H2β extraction and aromatization [10], and egress of water molecules and formic acid, the reaction byproducts. The other end of the channel is directed towards the lipid interface as depicted in Figure 6. The channel appears to serve as an aqueduct that connects the water reservoir at the lipid-protein interface to the catalytic site, and is topographically somewhat similar to the previously described “Channel 5” [39]. Ideally, the water molecules in the channel should be in dynamic equilibrium with an active enzyme and ought not to be “trapped” by strong interaction with protein atoms inside the channel. Accordingly, modeling of a continuous electron density inside the channel as discrete water molecules is an approximate representation of the experimental data that suggest it is a water-filled channel.

In conclusion, AROM has an androgen-specific substrate site where TST and ASD bind. It also has a defined heme proximal cavity and a binding scaffold provide solid evidence to this P450’s ability to interact with other non-steroidal molecular partners, some of which may have regulatory roles and/or exert allosteric effects on the enzyme activity. Whether this site can be targeted for designing small-molecule inhibitor/activator of AROM remains to be seen. X-ray data is used also to identify a previously uncharacterized aqueduct that stretches from the catalytic residues to the lipid interface charting a course for the passage of water molecules important in catalysis.

Supplementary Material

Refer to Web version on PubMed Central for supplementary material.

Acknowledgments

Funding

This work is supported, in whole or in part, by grant R01GM086893 from the National Institutes of Health and Carol M. Baldwin Breast Cancer Research Funds of Central New York. The Structural Biology Center at the Advanced Photon Source, Argonne, IL is operated by UChicago Argonne, LLC, for the U.S. Department of Energy, Office of Biological and Environmental Research under contract DE-AC02-06CH11357.

The authors wish to thank Jennifer Griswold Breen and Mary Erman for protein purification, crystallization, and assistance in data collection

References

1. Santen RJ, Brodie H, Simpson ER, Siiteri PK, Brodie A. History of aromatase: saga of an important biological mediator and therapeutic target. Endocrine reviews. 2009; 30(4):343–75. Epub 2009/04/25. DOI: 10.1210/er.2008-0016 [PubMed: 19389994]
2. Guengerich, FP. Cytochrome P450. Springer; 2005. Human cytochrome P450 enzymes; p. 377-530.

3. Simpson ER, Mahendroo MS, Means GD, Kilgore MW, Hinshelwood MM, Graham-Lorence S, et al. Aromatase cytochrome P450, the enzyme responsible for estrogen biosynthesis. Endocrine reviews. 1994; 15(3):342–55. Epub 1994/06/01. DOI: 10.1210/edrv-15-3-342 [PubMed: 8076586]

4. Akhtar M, Njar VC, Wright JN. Mechanistic studies on aromatase and related C-C bond cleaving P-450 enzymes. The Journal of steroid biochemistry and molecular biology. 1993; 44(4–6):375–87. Epub 1993/03/01. [PubMed: 8476751]

5. Chen S, Zhou D, Swiderek KM, Kadohama N, Osawa Y, Hall PF. Structure-function studies of human aromatase. The Journal of steroid biochemistry and molecular biology. 1993; 44(4–6):347–56. Epub 1993/03/01. [PubMed: 8476748]

6. Thompson EA Jr, Siiteri PK. The involvement of human placental microsomal cytochrome P-450 in aromatization. J Biol Chem. 1974; 249(17):5373–8. Epub 1974/09/10. [PubMed: 4370479]

7. Ryan KJ. Biological aromatization of steroids. J Biol Chem. 1959; 234(2):268–72. Epub 1959/02/01. [PubMed: 13630892]

8. Brodie AM, Marsh DA, Wu JT, Brodie HJ. Aromatase inhibitors and their use in controlling oestrogen-dependent processes. Journal of steroid biochemistry. 1979; 11(1A):107–12. [PubMed: 114710]

9. Brueggemeier RW, Hackett JC, Diaz-Cruz ES. Aromatase inhibitors in the treatment of breast cancer. Endocrine reviews. 2005; 26(3):331–45. Epub 2005/04/09. er.2004-0015 [pii]. DOI: 10.1210/er.2004-0015 [PubMed: 15814851]

10. Ghosh D, Griswold J, Erman M, Pangborn W. Structural basis for androgen specificity and oestrogen synthesis in human aromatase. Nature. 2009; 457(7226):219–23. Epub 2009/01/09. nature07614 [pii]. DOI: 10.1038/nature07614 [PubMed: 19129847]

11. Ghosh D, Griswold J, Erman M, Pangborn W. X-ray structure of human aromatase reveals an androgen-specific active site. The Journal of steroid biochemistry and molecular biology. 2010; 118(4–5):197–202. Epub 2009/10/08. S0960-0760(09)00240-4 [pii]. DOI: 10.1016/j.jsbmb.2009.09.012 [PubMed: 19808095]

12. Ghosh D, Jiang W, Lo J, Egbuta C. Higher order organization of human placental aromatase. Steroids. 2011; 76:753–8. Epub 2011/03/12. S0039-128X(11)00070-5 [pii]. DOI: 10.1016/j.steroids.2011.02.030 [PubMed: 21392520]

13. Ghosh, D., Lo, J., Egbuta, C. Resistance to Aromatase Inhibitors in Breast Cancer. Springer; 2015. Structure, Function and Inhibition of Aromatase; p. 33-61.

14. Jiang W, Ghosh D. Motion and Flexibility in Human Cytochrome P450 Aromatase. PloS one. 2012; doi: 10.1371/journal.pone.0032565

15. Lo J, Di Nardo G, Griswold J, Egbuta C, Jiang W, Gilardi G, et al. Structural basis for the functional roles of critical residues in human cytochrome p450 aromatase. Biochemistry. 2013; 52(34):5821–9. Epub 2013/08/01. DOI: 10.1021/bi400669h [PubMed: 23899247]

16. Akhtar M, Calder MR, Corina DL, Wright JN. Mechanistic studies on C-19 demethylation in oestrogen biosynthesis. The Biochemical journal. 1982; 201(3):569–80. Epub 1982/03/01. [PubMed: 7092812]

17. Sevrioukova IF, Li H, Zhang H, Peterson JA, Poulos TL. Structure of a cytochrome P450-redox partner electron-transfer complex. Proceedings of the National Academy of Sciences of the United States of America. 1999; 96(5):1863–8. Epub 1999/03/03. [PubMed: 10051560]

18. Catalano S, Barone I, Giordano C, Rizza P, Qi H, Gu G, et al. Rapid estradiol/ERalpha signaling enhances aromatase enzymatic activity in breast cancer cells. Mol Endocrinol. 2009; 23(10):1634–45. Epub 2009/06/27. me.2009–0039 [pii]. DOI: 10.1210/me.2009-0039 [PubMed: 19556341]

19. Barone I, Giordano C, Malivindi R, Lanzino M, Rizza P, Casaburi I, et al. Estrogens and PTP1B function in a novel pathway to regulate aromatase enzymatic activity in breast cancer cells. Endocrinology. 2012; 153(11):5157–66. Epub 2012/09/11. DOI: 10.1210/en.2012-1561 [PubMed: 22962253]

20. Egbuta C, Lo J, Ghosh D. Mechanism of inhibition of estrogen biosynthesis by azole fungicides. Endocrinology. 2014; 155(12):4622–8. [PubMed: 25243857]

21. Sgrignani J, Bon M, Colombo G, Magistrato A. Computational Approaches Elucidate the Allosteric Mechanism of Human Aromatase Inhibition: A Novel Possible Route to Small-

Molecule Regulation of CYP450s Activities? Journal of chemical information and modeling. 2014; 54(10):2856–68. [PubMed: 25178092]

22. Yoshida N, Osawa Y. Purification of human placental aromatase cytochrome P-450 with monoclonal antibody and its characterization. Biochemistry. 1991; 30(12):3003–10. Epub 1991/03/26. [PubMed: 2007137]
23. Lala P, Higashiyama T, Erman M, Griswold J, Wagner T, Osawa Y, et al. Suppression of human cytochrome P450 aromatase activity by monoclonal and recombinant antibody fragments and identification of a stable antigenic complex. The Journal of steroid biochemistry and molecular biology. 2004; 88(3):235–45. Epub 2004/05/04. S0960076004000159 [pii]. DOI: 10.1016/j.jsbmb.2003.12.010 [PubMed: 15120417]
24. Ghosh D, Lo J, Morton D, Valette D, Xi J, Griswold J, et al. Novel aromatase inhibitors by structure-guided design. Journal of medicinal chemistry. 2012; 55(19):8464–76. Epub 2012/09/07. DOI: 10.1021/jm300930n [PubMed: 22951074]
25. Otninowski, Z., Minor, W. HKL Manual. New Haven, Connecticut, USA: Yale University; 1995.
26. Murshudov GN, Vagin AA, Dodson EJ. Refinement of macromolecular structures by the maximum-likelihood method. Acta Crystallogr D Biol Crystallogr. 1997; 53:240–55. Epub 1997/05/01. S0907444996012255 [pii]. DOI: 10.1107/S0907444996012255 [PubMed: 15299926]
27. Emsley P, Cowtan K. Coot: model-building tools for molecular graphics. Acta Crystallogr D Biol Crystallogr. 2004; 60:2126–32. S0907444904019158 [pii]. DOI: 10.1107/S0907444904019158 [PubMed: 15572765]
28. Group, CC. Molecular Operating Environment (MOE). 10. Montreal, Canada: 2015.
29. Laurie AT, Jackson RM. Q-SiteFinder: an energy-based method for the prediction of protein-ligand binding sites. Bioinformatics. 2005; 21(9):1908–16. Epub 2005/02/11. DOI: 10.1093/bioinformatics/bti315 [PubMed: 15701681]
30. Dundas J, Ouyang Z, Tseng J, Binkowski A, Turpaz Y, Liang J. CASTp: computed atlas of surface topography of proteins with structural and topographical mapping of functionally annotated residues. Nucleic acids research. 2006; 34(Web Server issue):W116–8. Epub 2006/07/18. DOI: 10.1093/nar/gkl282 [PubMed: 16844972]
31. Pettersen EF, Goddard TD, Huang CC, Couch GS, Greenblatt DM, Meng EC, et al. UCSF Chimera--a visualization system for exploratory research and analysis. J Comput Chem. 2004; 25(13):1605–12. DOI: 10.1002/jcc.20084 [PubMed: 15264254]
32. DeLano, WL. The PyMOL molecular graphics system. San Carlos, CA, USA: DeLano Scientific; 2002.
33. Di Nardo G, Breitner M, Bandino A, Ghosh D, Jennings GK, Hackett JC, et al. Evidence for an elevated aspartate pKa in the active site of human aromatase. Journal of Biological Chemistry. 2015; 290(2):1186–96. [PubMed: 25425647]
34. Jones S, Thornton JM. Principles of protein-protein interactions. Proceedings of the National Academy of Sciences. 1996; 93(1):13–20.
35. Kulmacz RJ, Lands WEM. Stoichiometry and Kinetics of the Interaction of Prostaglandin H Synthase with Anti-inflammatory Agents. Journal of Biological Chemistry. 1985; 260(23):12572–8. [PubMed: 3930499]
36. Copeland RA, Williams JM, Giannaras J, Nurnberg S, Covington M, Pinto D, Pick S, Trzaskos JM. Mechanism of selective inhibition of the inducible isoform of prostaglandin G/H synthase. Proc Natl Acad Sci USA. 1994; 91:11202–6. [PubMed: 7972034]
37. Hong Y, Li H, Yuan YC, Chen S. Molecular characterization of aromatase. Ann N Y Acad Sci. 2009; 1155:112–20. Epub 2009/03/03. NYAS03703 [pii]. DOI: 10.1111/j.1749-6632.2009.03703.x [PubMed: 19250198]
38. Oprea TI, Hummer G, García AE. Identification of a functional water channel in cytochrome P450 enzymes. Proceedings of the National Academy of Sciences. 1997; 94(6):2133–8.
39. Cojocaru V, Winn PJ, Wade RC. The ins and outs of cytochrome P450s. Biochimica et biophysica acta. 2007; 1770(3):390–401. Epub 2006/08/22. DOI: 10.1016/j.bbagen.2006.07.005 [PubMed: 16920266]

Highlights

- First crystal structure of testosterone complex of human aromatase is reported
- Heme proximal region has a large surface cavity where polyethylene glycol binds
- Polyethylene glycol exhibits weak inhibition of aromatase activity
- The proximal cavity could serve as the site of interaction with other molecules
- The data also reveals a water channel from the active site to the lipid interface

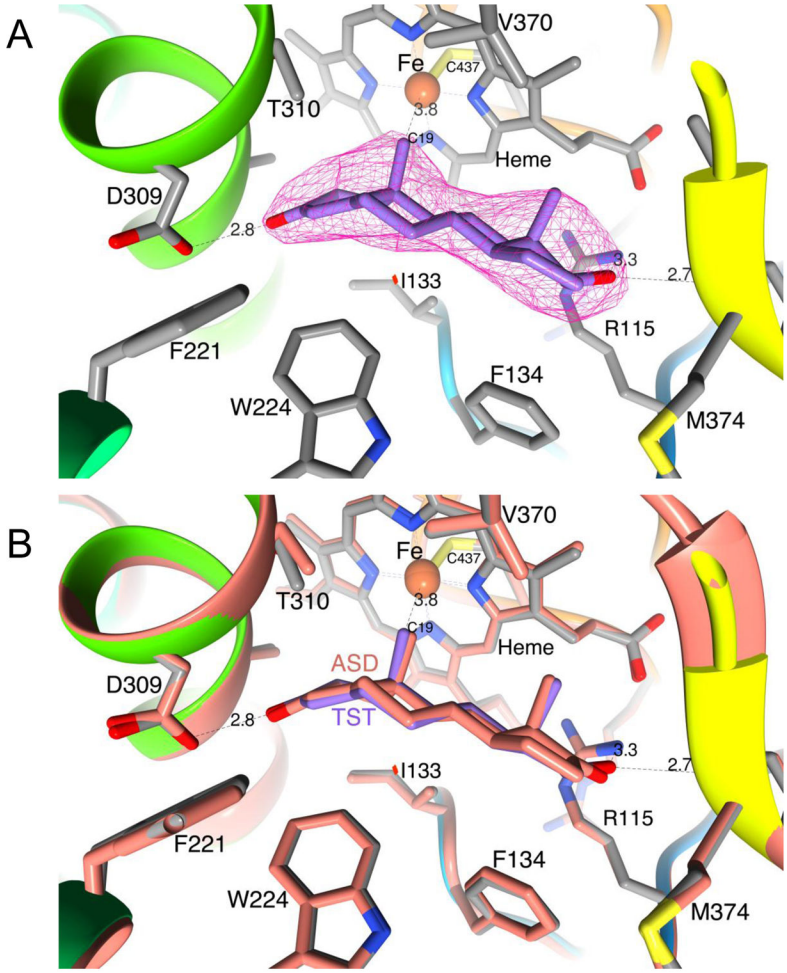

Figure 1. The active site cleft of pAROM-TST complex

(A) The bound TST molecule in the hemedistal cavity is shown within the omit difference electron density map contoured at 4.0σ. The residues that have polar and hydrophobic contacts with the substrate or in close proximity to the substrate are shown. The hydrogen bonds between the substrate and protein atoms, as well as heme Fe---C19 contact are indicated by dashed lines and distances are shown. The main chain ribbon is drawn in rainbow color – the N terminal in blue and C terminal is red. The residues are drawn in C: gray, O: red, N: blue, S: yellow, Fe: brick red. The carbon atoms TST are drawn in purple. **(B)** Superposition of the active sites of TST and ASD complexes of pAROM. The backbone and carbon atoms of the ASD complex are shown in salmon color.

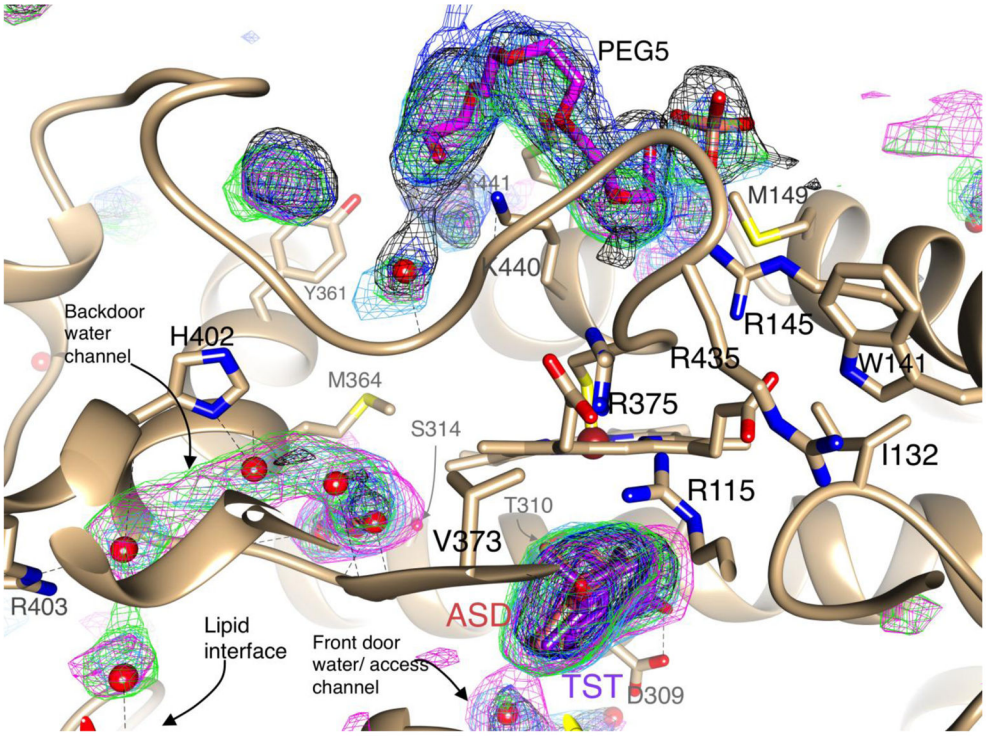

Figure 2. Superposition of omit difference electron density maps for the proximal and distal heme cavities of TST and ASD complexes of pAROM

A modeled PEG pentamer (PEG5) at the proximal density, the bound TST/ASD molecules at the distal substrate site and protein atoms for the ASD complex 1 at 2.75Å (Table 1) are shown. The electron density maps are color-coded, TST: green, ASD 1: black, ASD 2: blue, ASD 3: cyan, and ASD 4: magenta. The maps are contoured at 4.0 to 4.5σ. Important residues surrounding the cavities are also shown. Water molecules in front and back door channels are partially visible. Atom color codes are the same in all figures except carbon (C: beige for protein and heme, O: red, N: blue, S: yellow, P: orange).

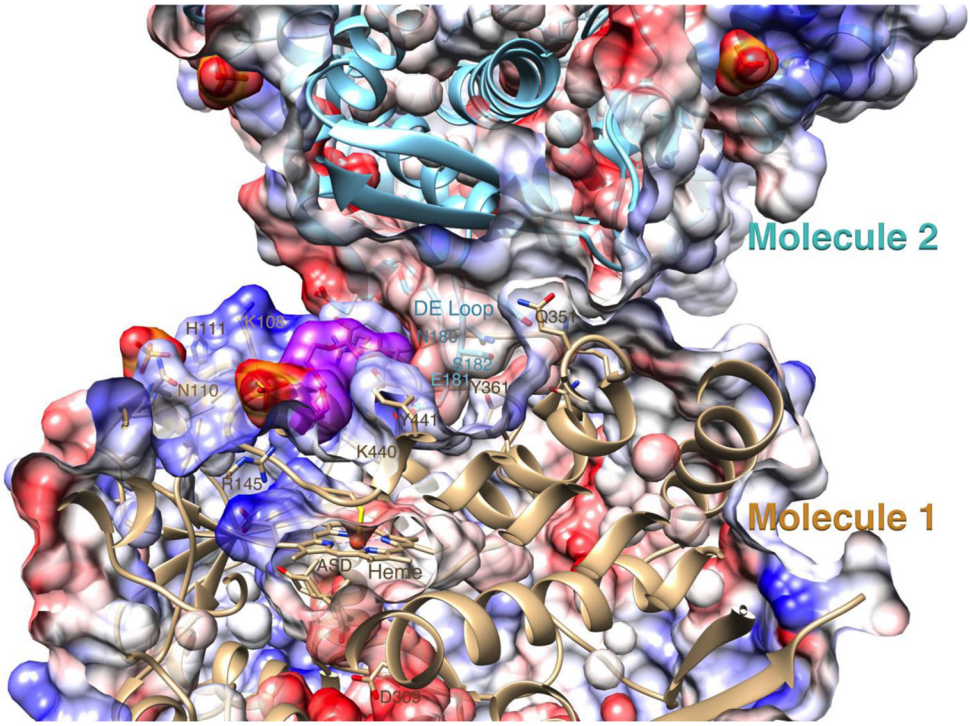

Figure 3. The proximal cavity and intermolecular association

Coulombic surfaces (colored red to blue: −10 to +10 kCal/mole) [31] of the head-to-tail dimer-forming Molecule 1 and Molecule 2 that are related by a crystallographic 3_2 symmetry are shown. The backbone ribbons and side chain carbon atoms are depicted in colors beige and cyan, respectively. The carbon atoms of PEG5 in the proximal cavity (of Molecule 1) and its van der Waals surface are depicted in magenta and purple, respectively. Slicing through the surface by a plane perpendicular to the viewing direction, the interior reveals the heme moiety, the distal ASD-binding site, the proximal PEG5-binding cleft and few key side chains. It also reveals the two-compartment nature of the proximal cavity, one that binds the D–E loop region of Molecule 2, and the other that scaffolds the PEG5 ligand. Phosphate ion binding sites are also shown.

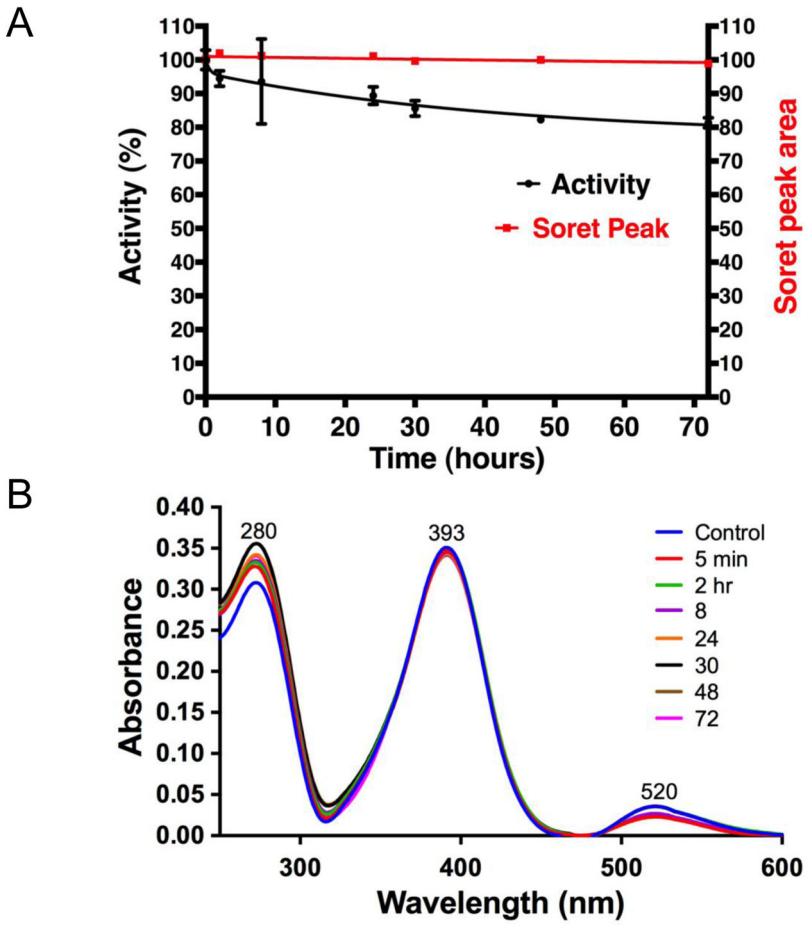

Figure 4. Time-dependent inhibition of enzyme activity in the presence of 10% PEG550

(**A**) The black curve represents least squares fit of the enzyme activity to the exponential decay equation. Inhibition plateaus at about 80% after 70 hours. The red line is the fit to the integrated area at different time points under the 393 nm Soret peak, which is virtually unchanged. (**B**) Superimposed Soret peaks at these time points are shown in the lower panel.

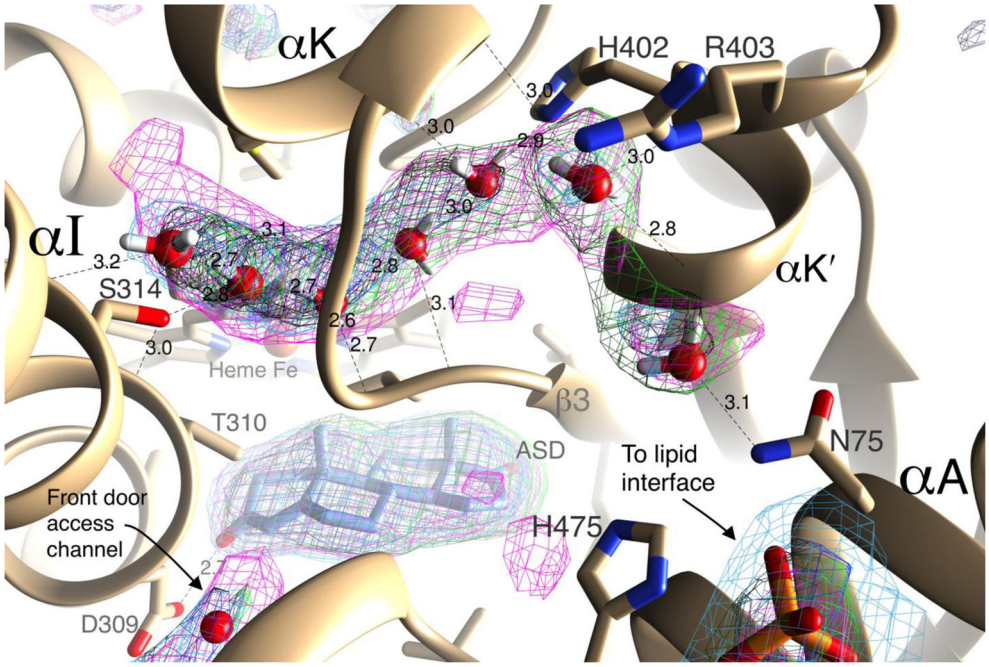

Figure 5. Superimposed omit difference electron density maps showing modeling of water molecules in the "backdoor" solvent channel

The electron density maps and the color-coding are the same as in Figure 2. The molecule displayed is the ASD complex 1 of AROM at 2.75Å resolution (Table 1). Hydrogen bonds are indicated by dashed lines and donor-acceptor distances in Å. Calculated hydrogen atoms for optimized waters are shown in light gray. Important side chains, secondary structure elements and the bound substrate are also labeled. Partially visible "front door" access channel and the lipid-protein interface with a bound phosphate moiety are indicated.

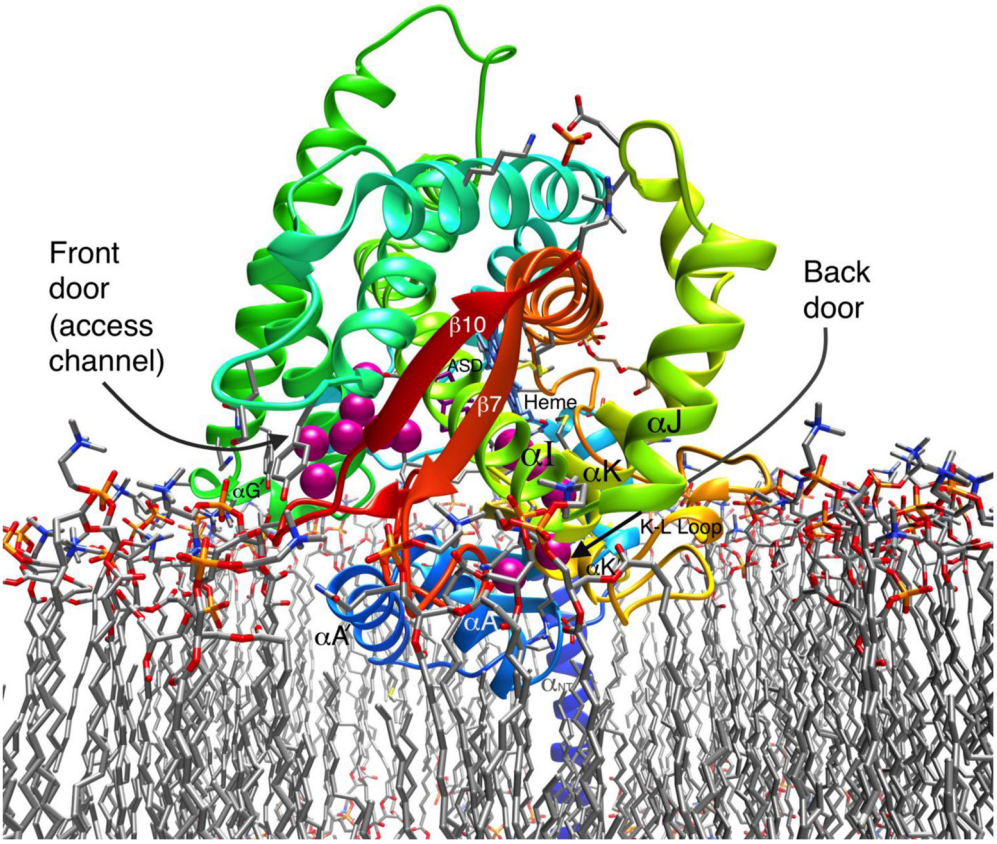

Figure 6. Orientations of the channels of pAROM in the lipid bilayer

The water molecules in the “front door” access channel and the newly identified “back door” channel are depicted in large magenta spheres to highlight the relative locations of the channels. The pAROM ribbon structure is drawn in rainbow colors: the N terminus in blue and the C terminus red. The lipid-embedded representation of pAROM is adapted from [14]; the N-terminal transmembrane helix is labeled α_{NT}. Partially visible ASD, heme, and lipid-associated structural elements are labeled (after the original description [10]).

J Steroid Biochem Mol Biol. Author manuscript; available in PMC 2019 July 01.

Table 1

Summary of X-ray data collection and refinement results

Complex/Crystal	pAROM-ASD1	pAROM-TST	pAROM-ASD2	pAROM-ASD3	pAROM-ASD4
PDB ID	5JKV	5JKW	5JL6	5JL7	5JL9
Data collection					
Space group	$P3_221$	$P3_221$	$P3_221$	$P3_221$	$P3_221$
Cell dimensions					
a=b, c (Å)	140.2, 119.2	140.9, 119.2	140.3, 118.4	140.3, 119.0	140.0, 119.4
α, β, γ (°)	90, 90, 120	90, 90, 120	90, 90, 120	90, 90, 120	90, 90, 120
Resolution range (Å)	121.43-2.75 (2.818-2.747)*	30.50-3.00 (3.077-3.000)	29.93-3.00 (3.076-2.999)	37.69-3.10 (3.1803.100)	37.81-3.10 (3.117-3.097)
R_{merge}	0.077 (0.79)	0.070 (0.55)	0.083 (0.95)	0.088 (0.80)	0.102 (0.93)
I/σI	25.4 (1.73)	23.3 (2.03)	25.8 (1.94)	24.2 (2.10)	22.0 (1.87)
Completeness (%)	99.5 (100)	95.7 (99.6)	98.2 (100)	97.7 (98.4)	99.0 (100)
Redundancy	6.0 (6.1)	3.6 (3.7)	4.2 (4.4)	4.5 (4.4)	4.5 (4.7)
*(highest resolution shell)					
Refinement					
Resolution (Å)	2.75	3.00	3.00	3.10	3.10
No. reflections	33634	24964	25528	23178	23538
R_{work}/R_{free}	0.214/0.236	0.20/0.22	0.20/0.22	0.18/0.21	0.19/0.21
No. atoms					
Protein	3668	3668	3668	3668	3668
Heme/Steroid	43/21	43/21	43/21	43/21	43/21
Polyethylene glycol	16	0	0	0	0
Water/Ion	43/20	7/0	7/0	7/0	7/0
B-factors (Å^2)					
Wilson plot	83.2	101.1	108.4	102.9	100.3
Mean	71.6	88.9	97.2	96.7	98.7
Protein	71.7	90.0	98.2	98.0	99.6
Heme/Steroid	47.2/50.1	64.2/63.8	71.7/73.4	67.9/72.8	72.5/78.7

Polyethylene glycol	108.7	No atoms	No atoms	No atoms	No atoms
Water	64.2	72.9	78.5	77.9	77.4
Phosphate ions	107.7	No atoms	No atoms	No atoms	No atoms
R.m.s deviations					
Bond lengths (Å)	0.008	0.008	0.008	0.008	0.008
Bond angles (°)	1.42	1.41	1.43	1.43	1.41
Overall coordinate error					
From R_{free} (Å)	0.22	0.27	0.26	0.27	0.27
Maxm. likelihood (Å)	0.18	0.20	0.21	0.21	0.21
Structure validation					
Φ/Ψ plot					
Favored region	425 (95.1%)	423 (94.6%)	419 (93.7%)	417 (93.3%)	420 (94.0%)
Allowed region	19 (4.3%)	20 (4.5%)	22 (4.9%)	23 (5.2%)	19 (4.3%)
Outlier region	3 (0.7%)	4 (0.9%)	6 (1.3%)	7 (1.6%)	8 (1.8%)
RMSD from highest resolution pArom-ASD structure					
C-alpha atoms (Å)	Not applicable	0.19	0.19	0.20	0.18
Side chain atoms (Å)	Not applicable	0.48	0.45	0.58	0.54

Table 2

Calculation of proximal cavity volume in P450's with known structures

CYP	Function	Size of heme-proximal cavity	Relative to AROM
Human AROM (CYP19A1)	Estrogen biosynthesis	584Å^3	-
Human CYP3A4	Oxidation of xenobiotics	659Å^3	1.1
Human CY46A1	24-hydroxylation of cholesterol	615Å^3	1.1
Human CYP11A1	Cholesterol side-chain cleavage	494Å^3	0.8
Human CYP2R1	Vitamin D 25-hydroxylase	477Å^3	0.8
Human CYP1A2	Xenobiotics metabolism	432Å^3	0.7
Human CYP2C8	Xenobiotics metabolism	394Å^3	0.7
Human CYP2A6	Xenobiotics metabolism	275Å^3	0.5
Human CYP2C9	Xenobiotics metabolism	197Å^3	0.3
Human CYP24A1	Degradation of 1,25dihydroxyvitamin D_3	185Å^3	0.3
Bacterial CYP101	Camphor hydroxylation	139 Å^3	0.2
Human CYP2A13	Xenobiotics metabolism	127Å^3	0.2
Human CYP51A1	Demethylation of lanosterol for fungal cell wall formation	88 Å^3	0.2
Rabbit CYP2C5	21-hydroxylation of steroids	66Å^3	0.1
Human CYP2B6, CYP2D6, CYP2E1, CYP8A1, CYP11B2, CYP17A1; Rabbit CYP2B4; Zebrafish CYP17A2; Mouse CYP21A1; Bacterial CYP102A1, CYP105, CYP105A1, CYP107H1, CYP108D1. CYP119. CYP120. CYP121, CYP124, CYP125, CYP130, CYP134A1, CYP142, CYP146A1, CYP152A1, CYP154C1, CYP158A2, CYP163B3, CYP167A1, CYP175A1, CYP231A2, P450OxyB	Steroid biosynthesis and xenobiotics metabolism	No well-defined cavity	0

Control used for Q-site computation: AROM active site volume: 395Å^3 (reported AROM active site volume: 400Å^3 [10]).